nature physics

Article

https://doi.org/10.1038/s41567-024-02638-2

A dual-species Rydberg array

Received: 31 May 2024

Accepted: 12 August 2024

Published online: 20 September 2024

Check for updates

Shraddha Anand[1,3], Conor E. Bradley[1,3], Ryan White[2], Vikram Ramesh[2], Kevin Singh[1] & Hannes Bernien[1]

Large-scale Rydberg atom arrays are used for highly coherent analogue quantum simulations and for digital quantum computations. However, advanced quantum protocols, such as quantum error correction, require midcircuit qubit operations, including the replenishment, reset and read-out of a subset of qubits. A compelling strategy for unlocking these capabilities is a dual-species architecture in which a second atomic species is controlled independently and entangled with the first through Rydberg interactions. Here, we realize a dual-species Rydberg array consisting of rubidium and caesium atoms and explore regimes of interactions and dynamics not accessible in single-species architectures. We achieve enhanced interspecies interactions by electrically tuning the Rydberg states close to a Förster resonance. In this regime, we demonstrate an interspecies Rydberg blockade and implement a quantum state transfer from one species to another. We then generate a Bell state between Rb and Cs hyperfine qubits through an interspecies controlled-phase gate. Finally, we combine interspecies entanglement with a native midcircuit read-out to achieve quantum non-demolition measurements.

Neutral atoms trapped in arrays of optical tweezers have recently been established as a front runner for both analogue quantum simulations and digital quantum computations[1–6]. The scalability of optical tweezer techniques has enabled systems with hundreds to thousands of atomic qubits[1,2,7–9]. Moreover, the development of efficient control schemes based on off-the-shelf optical components has led to the implementation of increasingly complex Hamiltonians and circuits[3,10–13]. Together with innovative approaches to error correction based on the multilevel nature of atomic qubits[14–17], these features have equipped neutral atom processors for exploring intermediate-scale quantum information science[18] and logical circuit operation[13].

The further development of this platform, however, requires solutions to outstanding challenges, which include repetitive midcircuit read-out (MCR) in large arrays[12,13,16,17,19–23] and the continuous replenishment of atoms lost during system operation[19,22,24–26]. These are essential for operating deep circuits and for auxiliary-qubit-assisted protocols, including quantum error correction[27]. A defining requirement for these challenges is that they must be performed with negligible crosstalk: 'auxiliary' qubits entangled with data qubits must be addressed without decohering the latter.

A promising strategy for achieving this requirement is to realize a dual-species Rydberg array[19,28–31] such that the unique addressing frequencies for each species result in independent control, crosstalk-free measurement[19] and straightforward methods for generating Rydberg-based entanglement between them. The intrinsic addressability of qubits allows for universal control schemes[32], efficient state preparation[33] and the study of new Hamiltonians[34,35], while maintaining a minimal control architecture of two separate global drives. Although previous demonstrations have shown Rydberg interactions between two atoms of different isotopes[29], an array of dual-species Rydberg atoms has yet to be demonstrated and would additionally benefit from using distinct atomic elements to dramatically suppress crosstalk.

In this article, we realize a dual-species Rydberg array composed of rubidium (Rb) and caesium (Cs) atoms. We show that, by choosing the Rydberg states and controlling the electric field, we can access both the van der Waals (vdW) and resonant dipole–dipole interaction regimes, the latter of which arises due to the presence of a hitherto unobserved interspecies Förster resonance[28]. We demonstrate a Rydberg blockade and show that independent control of the two species enables access to unexplored dynamical regimes in globally driven Rydberg arrays.

[1]Pritzker School of Molecular Engineering, University of Chicago, Chicago, IL, USA. [2]Department of Physics, University of Chicago, Chicago, IL, USA. [3]These authors contributed equally: Shraddha Anand, Conor E. Bradley. e-mail: bernien@uchicago.edu

https://doi.org/10.1038/s41567-024-02638-2

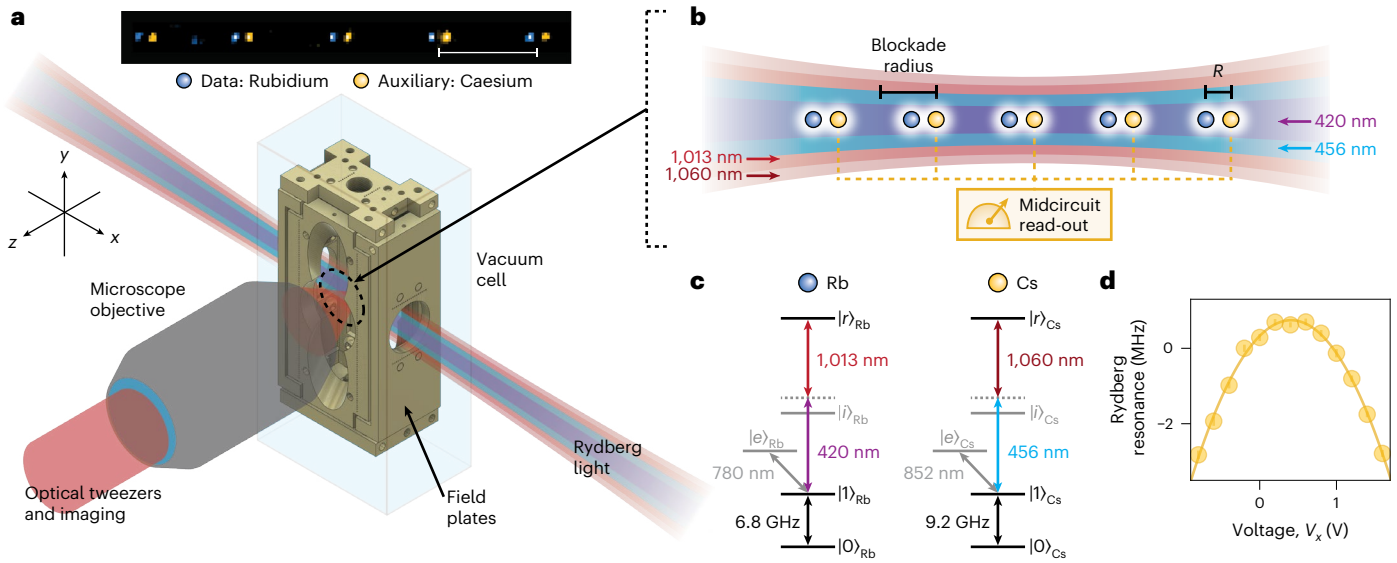

Fig. 1 | Rydberg interactions in a dual-species atom array. a, Example fluorescence image of the Rb–Cs atom array. Interspecies pairs (Rb–Cs) are separated by ~40 µm (indicated by the scale bar) to suppress crosstalk between adjacent couplets. Analogously, for intraspecies experiments (Rb–Rb and Cs–Cs), pairs were separated by ~25 µm. Experiments were performed inside an in-vacuum segmented Faraday cage that shields the atoms from stray electric fields and enables control of the electric field through the application of voltages to the electrically isolated field plates. **b**, The four Rydberg laser beams are focused onto the atom array to enable high Rydberg Rabi frequencies in a counter-propagating configuration that minimizes Doppler shifts. In the Rydberg state, Rb–Cs pairs experience dipolar interactions that are leveraged for interspecies entanglement. The spectral distinguishability between the atomic species enables crosstalk-free MCR of the Cs qubits. **c**, Atoms are excited to their respective Rydberg states by species-selective two-photon transitions. The qubits are encoded either in the gr $|1\rangle \leftrightarrow |r\rangle$ or the hf $|0\rangle \leftrightarrow |1\rangle$ manifold, with $|0\rangle_{Rb} = |F = 1, m_F = 0\rangle$, $|1\rangle_{Rb} = |2, 0\rangle$, $|0\rangle_{Cs} = |3, 0\rangle$ and $|1\rangle_{Cs} = |4, 0\rangle$, where F is the total angular momentum and m_F is the magnetic quantum number. The qubit is read out through fluorescence on the $|1\rangle \leftrightarrow |e\rangle$ transitions. **d**, The electric field at the position of the atoms is eliminated by applying voltages between pairs of field plates along each axis. The curve is an example Stark shift measurement of the $|1\rangle_{Cs} \leftrightarrow |r\rangle_{Cs}$ resonance arising from a voltage V_x applied along the x direction. Hereafter, unless stated otherwise, error bars are one standard error of the mean.

The blockade facilitates parallel controlled-phase (CZ) gates on pairs of hyperfine (hf) qubits, which allows us to generate interspecies Bell states. Finally, we demonstrate that these entangling operations are compatible with MCR by implementing auxiliary-based quantum non-demolition (QND) measurement with a read-out fidelity of 0.76(2) and a QND-ness of 0.94(2), without the need for qubit transport[13].

Our results showcase the richness of interaction regimes and dynamics that can be accessed in a dual-species tweezer-array architecture. Specifically, the interspecies Förster resonance provides anisotropic interactions for engineering many-body phases of matter[36,37], species-dependent interaction asymmetry for low-crosstalk and native multi-qubit gates[28,38–40], and beyond-nearest-neighbour connectivity[41]. Furthermore, the crosstalk-free and scalable control techniques offer exciting opportunities for new forms of quantum information processing[32] as well as efficient methods for creating long-range entangled states through measurement and feed-forward[42,43].

Dual-species Rydberg tweezer array

In our set-up, Rb and Cs atoms are cooled, trapped and imaged independently in optical tweezer arrays formed at the centre of an ultra-high vacuum glass cell[19,30]. The glass cell houses a segmented Faraday cage that allows control of the electric field in the environment (Fig. 1a and Supplementary Information Section 4). Apertures in the metal plates of the cage provide optical access. In this work, we focus on interactions between pairs of atoms trapped in a tweezer array.

Atoms are initialized in the hf clock states $|1\rangle_{Rb}$ and $|1\rangle_{Cs}$. Each species can then be independently excited to high-lying Rydberg S-states through species-selective two-photon transitions (Fig. 1b,c). We excite them to the $m_j = 1/2$ Rydberg states using frequency selectivity and polarization control, where m_j denotes the magnetic sublevel (Supplementary Information Section 3). The four Rydberg lasers are simultaneously locked to a single ultra-low expansion cavity to achieve narrow linewidths and suppress phase noise (Supplementary Information Section 3). As the laser frequencies that address these transitions are far-detuned from one another, the principal quantum number for the Rydberg states $|r\rangle_{Rb}$ and $|r\rangle_{Cs}$ can be chosen independently for the two species. This choice determines whether the atoms interact through dipole–dipole or vdW interactions ('Rydberg spectroscopy'). Qubits are encoded either in the ground-Rydberg (gr) manifold ($|1\rangle \leftrightarrow |r\rangle$) or in the hf manifold ($|0\rangle \leftrightarrow |1\rangle$). In the latter case, selective Rydberg excitation is still performed on the $|1\rangle \leftrightarrow |r\rangle$ transition, but single-qubit operations between the qubit states $|0\rangle$ and $|1\rangle$ are implemented by microwave driving[19]. During Rydberg operations, the tweezer light is turned off as Rydberg atoms experience an anti-trapping potential from the tweezers[44]. For gr encoding, the ramping up of tweezers is, thus, used to eject atoms in the Rydberg state. The remaining ground-state qubits can be detected through atomic fluorescence. Similarly, for the hf encoding, resonant light pulses ('pushout') are used to selectively remove atoms in $|1\rangle$. Finally, a midcircuit hf read-out can be performed on a subset of the qubits while dynamically decoupling the others (Supplementary Information Section 2).

Rydberg spectroscopy

We began by characterizing the Rydberg interaction strength between homogeneous and heterogeneous pairs of atoms. For Rb–Rb ($|r\rangle_{Rb} = |68S_{1/2}\rangle := |68\rangle$), Cs–Cs ($|r\rangle_{Cs} = |67S_{1/2}\rangle := |67\rangle$) and Rb–Cs pairs with the same principal quantum number ($|67, 67\rangle_{Rb,Cs}$), we expected vdW-type interactions that scale as $1/R^6$, where R is the interatomic spacing. Although the Rydberg interaction is fundamentally dipolar, this second-order scaling occurs due to significant non-degeneracy of Rydberg pair states[45] and is the typical regime used in atom arrays (Fig. 2a). For the interspecies case of $|68, 67\rangle_{Rb,Cs}$, however, there is a predicted coincidental near-degeneracy with another pair state, $|67P_{1/2}, 67P_{3/2}\rangle_{Rb,Cs}$, called a Förster resonance

https://doi.org/10.1038/s41567-024-02638-2

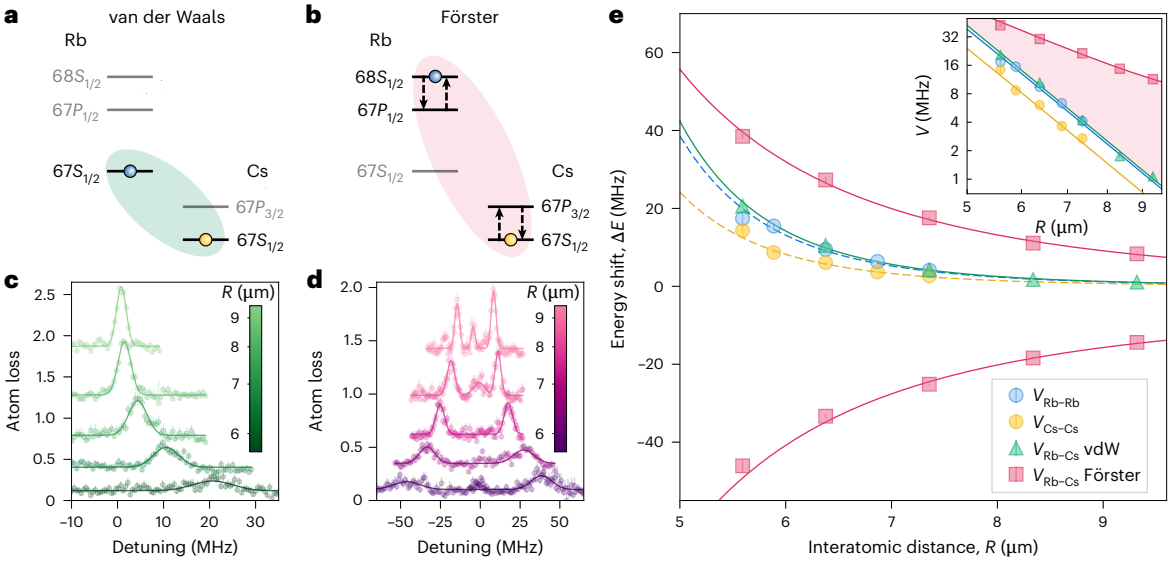

Fig. 2 | Förster versus vdW Rydberg interactions. a, Rb–Cs pairs excited to $|67S_{1/2}\rangle_{Rb}|67S_{1/2}\rangle_{Cs}$ interact through second-order vdW interactions (green). **b**, Rb–Cs pairs excited to $|68S_{1/2}\rangle_{Rb}|67S_{1/2}\rangle_{Cs}$ undergo resonantly enhanced Förster interactions (pink) due to near-degeneracy with the neighbouring pair state $|67P_{1/2}\rangle_{Rb}|67P_{3/2}\rangle_{Cs}$. **c**, The vdW interaction strength was extracted from the shift in the Rb Rydberg resonance after exciting the Cs atom to the Rydberg state. The strength increased with decreasing interatomic separation (see **e** for precise separation values). The vertical axis is offset for clarity, and the data were fitted to Gaussian profiles to extract the centres of the features. **d**, The Förster interaction strength was extracted similarly but reveals oher features. The two main peaks correspond to the eigenstates $|\pm\rangle_{pair}$ (see text). The smaller peaks at zero detuning correspond to the erroneous cases where the Cs atom was not excited to the Rydberg state. The centre peak at larger spacings stems from other resonant pair states, which can be suppressed by tuning the electric field (Supplementary Information Section 8). **e**, Measured energy shifts plotted against the interatomic spacing for the Rb–Rb, Cs–Cs and Rb–Cs vdW and Rb–Cs Förster interactions. The theoretically predicted (dashed) curves for the homogeneous pairs were used to calibrate the x axis. By fitting the heterogeneous pair data to the appropriate functional forms (solid lines, Supplementary Information Section 7), we found $C_3 = 16.4(3)$ GHz μm^3 and $C_6 = 662(21)$ GHz μm^6, both of which are compatible with theoretically predicted values. The inset shows the interaction strengths plotted on a log-log scale, which define $V = \Delta E$ for the vdW interactions and $V = (\Delta E_u - \Delta E_l)/2$ for the Förster interaction. Here, $\Delta E_{u(l)}$ denotes the energy of the upper (lower) branch. In **e**, error bars are statistical fit uncertainties.

(Fig. 2b), which would result in the re-emergence of resonant dipole–dipole interactions ($1/R^3$)[28]. As the resonance is sensitive to electric fields (Supplementary Information Section 6), we used the Faraday cage to nullify stray fields at the position of the atoms. This was achieved by maximizing the Rydberg transition energy (Fig. 1d).

For each combination of atomic states, we performed spectroscopy for several interatomic spacings ranging from 5.6 to 9.3 μm. Figure 2c,d shows the measured spectra when exciting the $|67, 67\rangle_{Rb,Cs}$ and $|68, 67\rangle_{Rb,Cs}$ transitions, respectively. We observed qualitatively distinct behaviour. In particular, a clear splitting of the spectrum was observed for the $|68, 67\rangle_{Rb,Cs}$. The two branches in the spectrum, corresponding approximately to the eigenstates

$$|\pm\rangle_{pair} = |68S_{1/2}\rangle_{Rb}|67S_{1/2}\rangle_{Cs} \pm |67P_{1/2}\rangle_{Rb}|67P_{3/2}\rangle_{Cs}, \quad (1)$$

confirm the presence of the near-degenerate Förster resonance[28,46–48]. In both cases, the interaction strength increased with proximity. A broadening of the resonances arose due to positional fluctuations from the finite temperature of the atoms[47,49].

When plotted against the interatomic spacing (Fig. 2e), we observed that, indeed, the Rb–Cs Förster interaction resulted in a slower fall-off than the Rb–Cs vdW interactions. By fitting the curves with the expected C_3/R^3 and C_6/R^6 functional forms (Supplementary Information Section 7), we extracted $C_3 = 16.4(3)$ GHz μm^3, and $C_6 = 662(21)$ GHz μm^6, which are compatible with the theoretically predicted values $C_3 = 15.66(2)$ GHz μm^3 and $C_6 = 745(1)$ GHz μm^6, where C_3 is the dipolar interaction coefficient and C_6 is the van der Waals coefficient (refs. 28,50). The minor disagreement probably arises from a percent-level discrepancy between the true and calibrated distance measurements and a residual angle (<2°) with the magnetic field (Supplementary Information Section 6). The interatomic spacing for the interspecies interactions was calibrated by fitting the measured intraspecies vdW interaction curves in Fig. 2e with the theoretically calculated values of C_6. Due to the isotropy and robustness to electric field noise of the vdW interactions and the availability of experimentally verified numerical tools for same-species interactions[50], this method provides a well-calibrated ruler for the distance between atoms.

These measurements constitute the observation of an interspecies Förster resonance between individually trapped atoms. The existence of such a resonance gives rise to a number of features including long-range interactions[10,51], anisotropy[36,52] and tunable interspecies and intraspecies interaction asymmetry (Supplementary Information Section 8)[28]. Indeed, even at modest trap spacings of 9.3 μm, we observed an asymmetry factor >10 between the interspecies Förster and intraspecies vdW interactions (Fig. 2e, inset).

Interspecies Rydberg blockade and dynamics

Operating at the Rb–Cs Förster pair resonance, we next employed coherent control of the gr qubit manifold to realize the interspecies blockade. For these experiments, pairs of atoms were placed at a distance of 5.6 μm. This resulted in an effective interspecies interaction strength of ~24 MHz (Supplementary Information Section 11), for which we expected strong blockade dynamics, that is the doubly excited state $|rr\rangle$ was shifted out of resonance (Fig. 3a).

To experimentally verify this, we used the independent addressability of the two species. We first applied a π pulse to the Rb qubits to excite them to $|r\rangle_{Rb}$ and then attempted to drive Rabi oscillations on the Cs $|1\rangle_{Cs} \leftrightarrow |r\rangle_{Cs}$ transition (Fig. 3b). The data collected were post-selected on loading pairs of atoms and on successful state preparation of the Rb qubit (Supplementary Information Section 9). We found that the amplitude of the Cs Rabi oscillation was dramatically suppressed in the presence of a Rb atom, a clear manifestation of the

https://doi.org/10.1038/s41567-024-02638-2

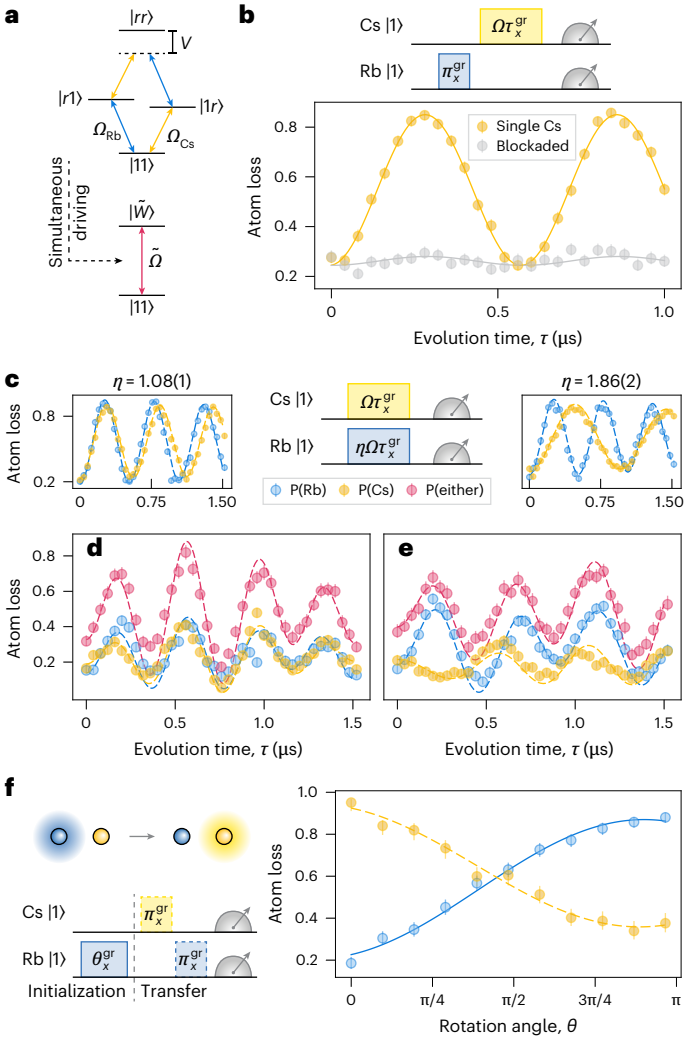

Fig. 3 | Dual-species Rydberg blockade and dynamics. a, Simplified Rb–Cs gr manifold level diagram depicting that the doubly excited state shifts out of resonance due to the Rydberg blockade. Under simultaneous driving, the ground state couples to a singly excited *W*-like state $|\tilde{W}\rangle$, with enhanced Rabi frequency $\tilde{\Omega}$ (Supplementary Information Section 13). **b**, Rb atoms were prepared in $|r\rangle$, followed by Rabi driving of the Cs atoms. Conditioning on single versus pair loading and the correct preparation of the Rb atom (Supplementary Information Section 9), the fitted Cs oscillation amplitude was strongly suppressed from $A = 0.606(18)$ to $A = 0.036(24)$. π_x denotes a π pulse around the *x*-axis. **c**, In the absence of the other species, Rb and Cs exhibit typical Rydberg Rabi oscillations. **d**,**e**, Observed and simulated Rydberg dynamics under simultaneous driving. **d**, The Rabi frequencies are balanced such that $\eta = \Omega_{Rb}/\Omega_{Cs} = 1.92(1)/1.78(1) = 1.08(1)$. **e**, The Rabi frequencies are unbalanced such that $\eta = 1.93(1)/1.04(1) = 1.86(2)$. When paired, enhanced oscillations occur at 2.53(2) MHz (**d**) and 2.17(2) MHz (**e**), as expected from $\tilde{\Omega}$. The relative excitation probability is theoretically given by $\Omega_i^2/\tilde{\Omega}^2$, $i \in \{\text{Rb, Cs}\}$. These observations are affected by SPAM errors but are described well by numerical simulations that taking these into account (dashed lines in **c**–**e**). **f**, For the interspecies quantum state transfer, the Rb atom is initialized in an arbitrary state through $R_x(\theta)$ (solid blue line). After initialization, a π pulse on Cs generates $\langle ZZ\rangle$ correlations, and a subsequent π pulse on Rb disentangles the atoms and completes the transfer (dashed yellow line).

Rydberg blockade. The data presented here were not corrected for the remaining state-preparation and measurement (SPAM) errors, which are the dominant limitations on the contrast of the Rabi oscillations. To minimize contributions from atoms not in $|1\rangle$, we converted these errors to loss (erasure) by a state-selective pushout before any Rydberg driving (Supplementary Information Section 9).

A second indicator of blockade physics is the observation of enhanced Rabi oscillations between the fully occupied ground state and a collective singly excited state[49,53–55]. For *N* blockaded atoms undergoing collective driving, the single-atom Rabi frequency is enhanced by $\sqrt{N}$, whereas the maximal single-atom excitation probability is given by $1/N$. With independent drives on each species, however, a richer variety of dynamics can be accessed. Considering two atoms with Rabi frequencies Ω_1 and Ω_2, enhanced oscillations now occur at a collective frequency $\tilde{\Omega} = \sqrt{\Omega_1^2 + \Omega_2^2}$, whereas the maximal excitation probability on each site is given by $\Omega_i^2/\tilde{\Omega}^2$, $i \in \{1, 2\}$ (Supplementary Information Section 13). Here, we demonstrate these phenomena.

Figure 3c shows the single-atom $|1\rangle \leftrightarrow |r\rangle$ Rabi oscillations. In contrast, for Fig. 3d,e, we performed collective driving on pairs of Rb and Cs qubits. For the interspecies case of Rb–Cs pairs, we varied the ratio of the Rabi frequencies. When the Rabi frequencies were balanced to within 10% ($\eta = \Omega_{Rb}/\Omega_{Cs} = 1.08(1)$, Fig. 3d), we observed the expected $\tilde{\Omega}$ and found that the excitation probabilities were comparable, with a minor enhancement in favour of Rb. Conversely, for a significantly imbalanced case ($\eta = 1.86(2)$, Fig. 3e), it was significantly more probable that the excitation was found on the Rb atom. For Rb–Rb and Cs–Cs pairs, we recovered the expected $\sqrt{2}$ enhancement in the Rabi frequency, with an accompanying reduction in the single-site excitation probability (Supplementary Information Section 12). Incorporating SPAM errors, our data are described well by numerical simulations without any free parameters (Supplementary Information Section 11). We expect a significant reduction in SPAM errors with future experimental upgrades.

Having established the interspecies Rydberg blockade, we next showed that this enables new approaches to multi-qubit protocols, in particular, quantum state transfer. Here, a variable rotation $R_x(\theta)$ prepared an arbitrary Rb gr superposition state (Fig. 3f, 'Initialization'). Then, π pulses were applied to the Cs and Rb qubits in turn. In the blockade regime, this pulse sequence resulted in the transfer of the Rb state to the Cs qubit (Fig. 3f, 'Transfer'), as indicated here by the generation of $\langle ZZ\rangle$ correlations (Supplementary Information Section 14). The species-selective Rydberg excitation, thus, enabled simple pulse schemes for quantum information processing, all within an architecture composed of global Rydberg drives. For instance, such techniques can be used for auxiliary-enhanced Rydberg state detection and for controlling the spatial flow of quantum information[32].

These demonstrations highlight the unexplored dynamical regimes and information processing protocols available in collectively driven dual-species Rydberg arrays[32,34,35]. With straightforward adjustments of the array geometry, laser detunings or laser intensities, subsets of the atomic array can be engineered to have different dynamics from the rest without the need for local addressing[10,56].

Two-qubit gate and MCR

We next extended the quantum correlations generated by the Rb–Cs blockade to the hf qubit manifold and demonstrated interspecies logic operations in an atom array. To perform the entangling operations, we used the 'π-2π-π' protocol[57], with the π pulses performed on Cs and the intermediary 2π pulse performed on Rb. If the first π pulse excites the Cs qubit to the Rydberg state, the Rb qubit is blockaded and remains unaffected; otherwise, it acquires a geometric phase of π. This allowed us to engineer a CZ gate. To verify this, the Rb qubits were prepared in the superposition state $|-\rangle_{Rb} = (|0\rangle_{Rb} - |1\rangle_{Rb})/\sqrt{2}$, the Cs qubits were prepared in each of the two eigenstates $|0\rangle_{Cs}$ or $|1\rangle_{Cs}$, and the π-2π-π scheme was applied. Measuring the phase accrued by the Rb qubits resulted in an 'eye diagram' (Fig. 4a) with a conditional phase of 1.01(1) π as desired. Throughout these hf-manifold measurements, we built on refs. 16,39 to develop a straightforward method for correcting SPAM errors at the cost of reduced raw fidelities by converting most of these to loss (Supplementary Information Section 9).

https://doi.org/10.1038/s41567-024-02638-2

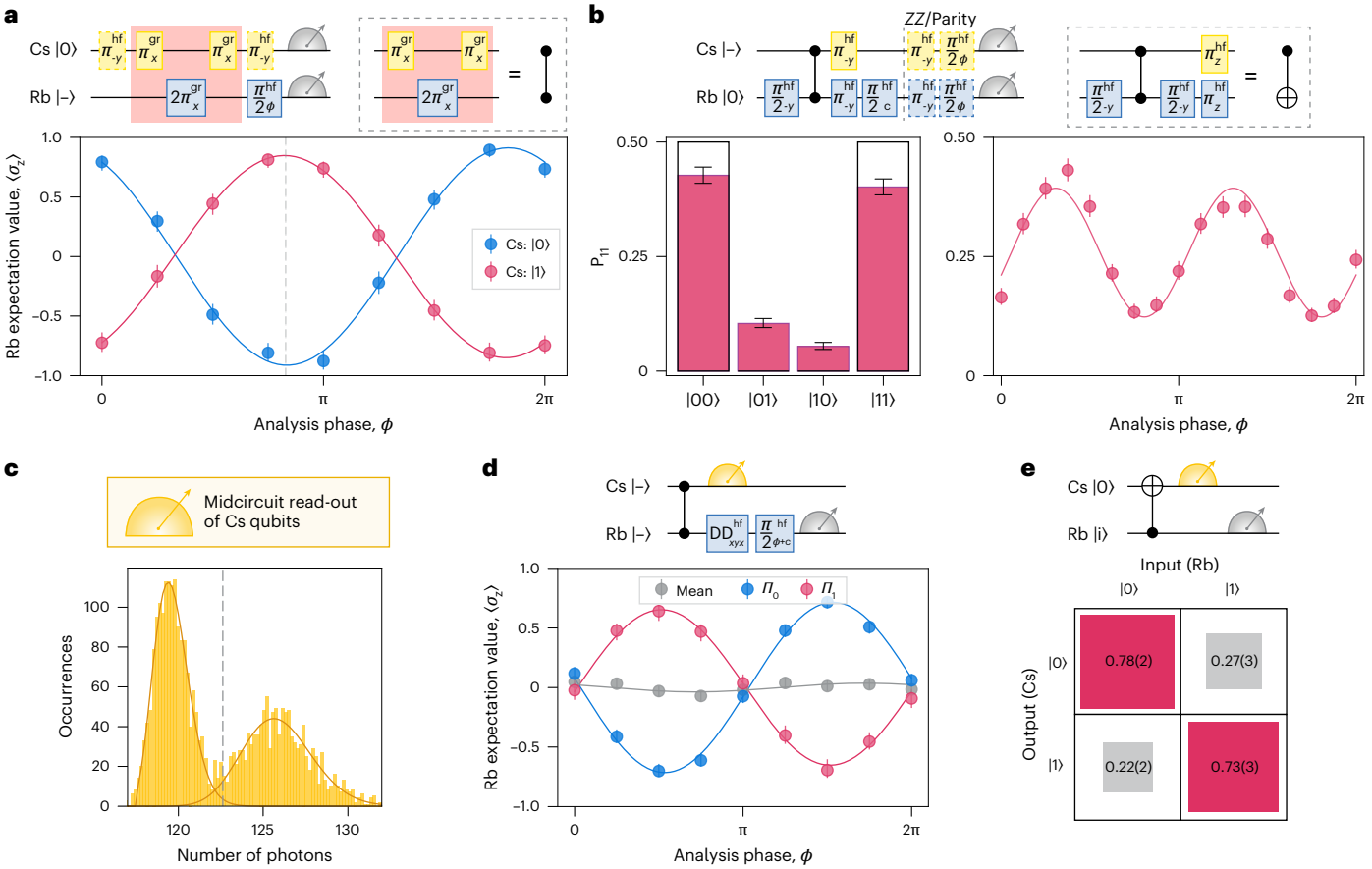

Fig. 4 | Entanglement of long-lived hf qubits and midcircuit QND read-out. **a**, Measurement of the conditional phase accrued by Rb atoms undergoing a π-2π-π sequence (eye diagram). The Cs atoms were prepared in the eigenstates $|0\rangle$ or $|1\rangle$ (dashed boxes). The conditional phase was 1.01(1)π, and the SPAM-corrected contrast was 0.88(1). The gr pulses implemented a hf CZ gate up to single-qubit phases. The dashed grey line indicates the point of maximal contrast. Spin echoes (π^{hf}_{-y}) are incorporated to mitigate hf dephasing, with π pulses around the −y axis. **b**, Parallel preparation of the canonical Bell state $|\Psi^+\rangle$ across several Rb–Cs pairs. By measuring the populations and coherences (dashed boxes), we extracted an average SPAM-corrected Bell state fidelity of $\mathcal{F}_{\mathrm{Bell}} = 0.69(3)$. The combination of hf π/2-pulses and gr pulses realized a CNOT operation up to single-qubit rotations. The phase correction c corresponds to the point of maximal contrast in **a**. **c**, Example Cs MCR histogram as used for **d** and **e** (7 ms fluorescence; Supplementary Information Section 2). The fitted discrimination fidelity was 0.990(3). **d**, After preparing the Bell state $|\Psi^x\rangle$ (see text), the MCR of the Cs atoms projects the two-qubit state. Conditioning on the measurement outcomes reveals $\langle ZX\rangle_{\mathrm{Cs,Rb}}$ correlations, which confirm that the Rb coherence survives MCR. The conditional phase was 1.02(1)π, and the SPAM-corrected contrast was 0.68(1). DD denotes dynamical decoupling, and $\Pi_{0(1)}$ denotes measurement of the 0(1) outcome on the Cs qubit. **e**, Auxiliary-based QND measurement of the Rb qubit through the Cs qubit. The read-out fidelity was extracted as $\mathcal{F}_{\mathrm{QND}} = 0.76(2)$.

With the interspecies two-qubit gate, we could next generate a maximally entangled Bell state. We prepared both species in the $|-\rangle$ state, performed the entangling sequence and then applied a single-qubit $R_\phi(\pi/2)$ gate on the Rb qubit, with ϕ set to the point of maximum contrast in Fig. 4a. Assessing the Bell state by measuring the two-qubit populations and coherences (Fig. 4b), we clearly observed the expected correlations in the populations alongside the enhanced frequency associated with parity oscillations of an entangled state. The Bell state fidelity was evaluated to be $\mathcal{F}_{\mathrm{Bell}} = 0.69(3)$ after correcting for SPAM errors (raw fidelity $\mathcal{F}^{\mathrm{raw}}_{\mathrm{Bell}} = 0.49(2)$). We, thus, demonstrated Rydberg blockade-based entanglement of two different atomic species. The measured SPAM-corrected fidelity is in good agreement with our error model, which predicted $\mathcal{F}^{\mathrm{sim}}_{\mathrm{Bell}} = 0.73$ (Supplementary Information Section 11). The fidelity was predominantly limited by two dephasing mechanisms: gr T_2^* of the idling Cs atom (estimated infidelity $\epsilon^{\mathrm{gr}}_{T_2^*} = 0.20$) and the hf-manifold dephasing of both species from differential Stark shifts induced by the blue light ($\epsilon^{\mathrm{hf}}_{\mathrm{Stark}} = 0.04$). The latter could be suppressed by balancing the single-photon Rabi frequencies, whereas the former was probably limited by laser phase noise, which could be addressed by technical upgrades[44,58–60] or by using continuous-driving gate schemes[61,62]. Such technical improvements will enable higher gate fidelities, comparable to those achieved recently in both alkaline and alkaline-earth atom arrays[16,63,64].

In a final pair of measurements, we combined the interspecies two-qubit gates with the MCR capabilities of the dual-species architecture (Fig. 4c)[19]. First, we demonstrated the ability to perform projective measurements on a subcomponent of an entangled state. After preparing the Bell state $|\Psi^x\rangle_{\mathrm{Cs,Rb}} := (|0+\rangle + |1-\rangle)/\sqrt{2}$, we performed MCR on the Cs qubit, during which the Rb qubit was decoupled. Once the MCR was complete, we measured the Rb coherence by sweeping the phase of a final π/2 pulse (Fig. 4d). Conditioning on the MCR outcomes revealed the coherent oscillations associated with the eye diagram of Fig. 4a. Hence, the Cs MCR projected the Rb state without any further decoherence.

Second, we implemented QND detection of the Rb state by using Cs as an auxiliary qubit. The quantum circuit is shown in Fig. 4e. After preparing the Rb qubit in a chosen eigenstate, we inserted the CZ gate between a pair of π/2 pulses on the Cs qubit, performed the MCR of the Cs and then read out the Rb state. The conditional phase induced by the CZ gate correlated the Cs read-out outcome with the Rb state, which was minimally perturbed in the process. Quantitatively, the QND-ness of the measurement—the probability that the input state of the data

qubit was unperturbed by the read-out—was measured to be 0.94(2) (Supplementary Information Section 10). We extracted a QND read-out fidelity $\mathcal{F}_{\mathrm{QND}} = (\mathcal{F}_{0|0} + \mathcal{F}_{1|1})/2 = 0.76(2)$, in good agreement with our numerical model (predicted $\mathcal{F}_{\mathrm{QND}} = 0.78$). Note that $\mathcal{F}_{\mathrm{QND}}$ was predominantly limited by dephasing of the auxiliary qubit during the two-qubit gate rather than decoherence of the data qubit. Accordingly, the much higher QND-ness could enable improved $\mathcal{F}_{\mathrm{QND}}$ through several rounds of repetitive read-out[65]. This could be achieved by either reloading lost auxiliary qubits[19,22] or by imaging the auxiliary qubits in a non-destructive fashion[66].

This demonstration of interspecies gates and entanglement in an optical tweezer array is an essential prerequisite for advanced quantum algorithms in a dual-species quantum processor. Together with the extension of the auxiliary-qubit-based QND protocol to larger numbers of qubits, our approach will enable the exploration of quantum feedback control, error correction[27], measurement-based state preparation[42,43] and the measurement-based paradigm of quantum computing[67].

Discussion

This work introduces the dual-species Rydberg architecture and establishes it as a powerful tool, both for quantum information science and for accessing new regimes in many-body physics. By integrating strong Rydberg interactions with the native addressability intrinsic to this approach, we have shown that a dual-species system is a natural setting in which to implement auxiliary-qubit-based protocols such as QND measurements. In combination with our recent demonstration of midcircuit feed-forward and read-out in two-dimensional arrays and of coherent replenishment of atoms during circuit operation[19], dual-species Rydberg arrays are poised to explore quantum error correction and the generation of long-range entangled states[42,43] in large systems. Although improvements in operation fidelities will be required, the necessary technical upgrades are well understood[44,64]. The further addition of fast Raman-based single-qubit operations[68], local-addressing techniques[3,10–13] and non-destructive read-out[69,70] will enable increasingly complex protocols.

Additionally, the independent addressability of the two species and the richness of interspecies Rydberg physics together provide the means to both extend the set of implementable Hamiltonians[34,35] and prepare a wide range of quantum states that are challenging to access in globally driven single-species arrays. The experimental confirmation of interelement Rydberg Förster resonances offers long-range interactions[71] and the ability to tune the interspecies and intraspecies interaction asymmetry. This, in turn, gives rise to strategies for modifying qubit connectivity, exploring complex models in quantum many-body physics[36,37] and directly implementing multi-qubit gates[33,38–40]. The Förster interaction itself can be switched on and off on nanosecond timescales using the electric field control available in our set-up[47], which could be utilized for Floquet engineering[72,73]. The dual-species neutral atom platform thus has a dual advantage: it provides access to both a wider variety of quantum phenomena and it is a versatile control toolbox for leveraging them for quantum information science.

Online content

Any methods, additional references, Nature Portfolio reporting summaries, source data, extended data, supplementary information, acknowledgements, peer review information; details of author contributions and competing interests; and statements of data and code availability are available at https://doi.org/10.1038/s41567-024-02638-2.

References

1. Scholl, P. et al. Quantum simulation of 2D antiferromagnets with hundreds of Rydberg atoms. *Nature* **595**, 233–238 (2021).
2. Ebadi, S. et al. Quantum phases of matter on a 256-atom programmable quantum simulator. *Nature* **595**, 227–232 (2021).
3. Graham, T. et al. Multi-qubit entanglement and algorithms on a neutral-atom quantum computer. *Nature* **604**, 457–462 (2022).
4. Bluvstein, D. et al. A quantum processor based on coherent transport of entangled atom arrays. *Nature* **604**, 451–456 (2022).
5. Browaeys, A. & Lahaye, T. Many-body physics with individually controlled Rydberg atoms. *Nat. Phys.* **16**, 132–142 (2020).
6. Kaufman, A. & Ni, K. Quantum science with optical tweezer arrays of ultracold atoms and molecules. *Nat. Phys.* **17**, 1324–1333 (2021).
7. Huft, P. et al. Simple, passive design for large optical trap arrays for single atoms. *Phys. Rev. A* **105**, 063111 (2022).
8. Pause, L. et al. Supercharged two-dimensional tweezer array with more than 1000 atomic qubits. *Optica* **11**, 222–226 (2024).
9. Tao, R., Ammenwerth, M., Gyger, F., Bloch, I. & Zeiher, J. High-fidelity detection of large-scale atom arrays in an optical lattice. *Phys. Rev. Lett.* **133**, 013401 (2024).
10. Chen, C. et al. Continuous symmetry breaking in a two-dimensional Rydberg array. *Nature* **616**, 691–695 (2023).
11. Shaw, A. et al. Multi-ensemble metrology by programming local rotations with atom movements. *Nat. Phys.* **20**, 195–201 (2024).
12. Lis, J. et al. Midcircuit operations using the *omg* architecture in neutral atom arrays. *Phys. Rev. X* **13**, 041035 (2023).
13. Bluvstein, D. et al. Logical quantum processor based on reconfigurable atom arrays. *Nature* **626**, 58–65 (2024).
14. Wu, Y., Kolkowitz, S., Puri, S. & Thompson, J. Erasure conversion for fault-tolerant quantum computing in alkaline earth Rydberg atom arrays. *Nat. Commun.* **13**, 4657 (2022).
15. Cong, I. et al. Hardware-efficient, fault-tolerant quantum computation with Rydberg atoms. *Phys. Rev. X* **12**, 021049 (2022).
16. Ma, S. et al. High-fidelity gates and mid-circuit erasure conversion in an atomic qubit. *Nature* **622**, 279–284 (2023).
17. Scholl, P. et al. Erasure conversion in a high-fidelity Rydberg quantum simulator. *Nature* **622**, 273–278 (2023).
18. Shaw, A. et al. Benchmarking highly entangled states on a 60-atom analogue quantum simulator. *Nature* **628**, 71–77 (2024).
19. Singh, K. et al. Mid-circuit correction of correlated phase errors using an array of spectator qubits. *Science* **380**, 1265–1269 (2023).
20. Deist, E. et al. Mid-circuit cavity measurement in a neutral atom array. *Phys. Rev. Lett.* **129**, 203602 (2022).
21. Graham, T. et al. Midcircuit measurements on a single-species neutral alkali atom quantum processor. *Phys. Rev. X* **13**, 041051 (2023).
22. Norcia, M. et al. Midcircuit qubit measurement and rearrangement in a ^{171}Yb atomic array. *Phys. Rev. X* **13**, 041034 (2023).
23. Huie, W. et al. Repetitive readout and real-time control of nuclear spin qubits in ^{171}Yb atoms. *PRX Quantum* **4**, 030337 (2023).
24. Pause, L., Preuschoff, T., Schäffner, D., Schlosser, M. & Birkl, G. Reservoir-based deterministic loading of single-atom tweezer arrays. *Phys. Rev. Res.* **5**, L032009 (2023).
25. Norcia, M. et al. Iterative assembly of ^{171}Yb atom arrays in cavity-enhanced optical lattices. *PRX Quantum* **5**, 030316 (2024).
26. Gyger, F. et al. Continuous operation of large-scale atom arrays in optical lattices. *Phys. Rev. Res.* **6**, 033104 (2024).
27. Terhal, B. Quantum error correction for quantum memories. *Rev. Mod. Phys.* **87**, 307 (2015).
28. Beterov, I. & Saffman, M. Rydberg blockade, Förster resonances, and quantum state measurements with different atomic species. *Phys. Rev. A* **92**, 042710 (2015).
29. Zeng, Y. et al. Entangling two individual atoms of different isotopes via Rydberg blockade. *Phys. Rev. Lett.* **119**, 160502 (2017).
30. Singh, K., Anand, S., Pocklington, A., Kemp, J. & Bernien, H. Dual-element, two-dimensional atom array with continuous-mode operation. *Phys. Rev. X* **12**, 011040 (2022).
31. Sheng, C. et al. Defect-free arbitrary-geometry assembly of mixed-species atom arrays. *Phys. Rev. Lett.* **128**, 083202 (2022).

32. Cesa, F. & Pichler, H. Universal quantum computation in globally driven Rydberg atom arrays. *Phys. Rev. Lett.* **131**, 170601 (2023).
33. Müller, M., Lesanovsky, I., Weimer, H., Büchler, H. & Zoller, P. Mesoscopic Rydberg gate based on electromagnetically induced transparency. *Phys. Rev. Lett.* **102**, 170502 (2009).
34. Homeier, L. et al. Realistic scheme for quantum simulation of Z_2 lattice gauge theories with dynamical matter in (2+1)D. *Commun. Phys.* **6**, 127 (2023).
35. Chepiga, N. Tunable quantum criticality in multicomponent Rydberg arrays. *Phys. Rev. Lett.* **132**, 076505 (2024).
36. de Léséleuc, S. et al. Observation of a symmetry-protected topological phase of interacting bosons with Rydberg atoms. *Science* **365**, 775–780 (2019).
37. Kim, K., Yang, F., Mølmer, K. & Ahn, J. Realization of an extremely anisotropic Heisenberg magnet in Rydberg atom arrays. *Phys. Rev. X* **14**, 011025 (2024).
38. Khazali, M. & Mølmer, K. Fast multiqubit gates by adiabatic evolution in interacting excited-state manifolds of Rydberg atoms and superconducting circuits. *Phys. Rev. X* **10**, 021054 (2020).
39. McDonnell, K., Keary, L. & Pritchard, J. Demonstration of a quantum gate using electromagnetically induced transparency. *Phys. Rev. Lett.* **129**, 200501 (2022).
40. Farouk, A., Beterov, I., Xu, P., Bergamini, S. & Ryabtsev, I. Parallel implementation of $CNOT^N$ and C_2NOT^2 gates via homonuclear and heteronuclear Förster interactions of Rydberg atoms. *Photonics* **10**, 1280 (2023).
41. Baker, J. et al. Exploiting long-distance interactions and tolerating atom loss in neutral atom quantum architectures. In *Proc. 2021 ACM/IEEE 48th Annual ISCA* 818–831 (IEEE, 2021).
42. Lu, T., Lessa, L., Kim, I. & Hsieh, T. Measurement as a shortcut to long-range entangled quantum matter. *PRX Quantum* **3**, 040337 (2022).
43. Iqbal, M. et al. Topological order from measurements and feed-forward on a trapped ion quantum computer. *Commun. Phys.* **7**, 205 (2024).
44. de Léséleuc, S., Barredo, D., Lienhard, V., Browaeys, A. & Lahaye, T. Analysis of imperfections in the coherent optical excitation of single atoms to Rydberg states. *Phys. Rev. A* **97**, 053803 (2018).
45. Browaeys, A., Barredo, D. & Lahaye, T. Experimental investigations of dipole–dipole interactions between a few Rydberg atoms. *J. Phys. B: At. Mol. Opt. Phys.* **49**, 152001 (2016).
46. Comparat, D. & Pillet, P. Dipole blockade in a cold Rydberg atomic sample. *J. Opt. Soc. Am. B* **27**, A208–A232 (2010).
47. Ravets, S. et al. Coherent dipole-dipole coupling between two single Rydberg atoms at an electrically-tuned Förster resonance. *Nat. Phys.* **10**, 914–917 (2014).
48. Chew, Y. et al. Ultrafast energy exchange between two single Rydberg atoms on a nanosecond timescale. *Nat. Photonics* **16**, 724–729 (2022).
49. Bernien, H. et al. Probing many-body dynamics on a 51-atom quantum simulator. *Nature* **551**, 579–584 (2017).
50. Weber, S. et al. Tutorial: calculation of Rydberg interaction potentials. *J. Phys. B: At. Mol. Opt. Phys.* **50**, 133001 (2017).
51. Bornet, G. et al. Scalable spin squeezing in a dipolar Rydberg atom array. *Nature* **621**, 728–833 (2023).
52. Ravets, S., Labuhn, H., Barredo, D., Lahaye, T. & Browaeys, A. Measurement of the angular dependence of the dipole-dipole interaction between two individual Rydberg atoms at a Förster resonance. *Phys. Rev. A* **92**, 020701 (2015).
53. Gaëtan, A. et al. Observation of collective excitation of two individual atoms in the Rydberg blockade regime. *Nat. Phys.* **5**, 115–118 (2009).
54. Zeiher, J. et al. Microscopic characterization of scalable coherent Rydberg superatoms. *Phys. Rev. X* **5**, 031015 (2015).
55. Labuhn, H. et al. Tunable two-dimensional arrays of single Rydberg atoms for realizing quantum Ising models. *Nature* **534**, 667–670 (2016).
56. Omran, A. et al. Generation and manipulation of Schrödinger cat states in Rydberg atom arrays. *Science* **365**, 570–574 (2019).
57. Jaksch, D. et al. Fast quantum gates for neutral atoms. *Phys. Rev. Lett.* **85**, 2208 (2000).
58. Endo, M. & Schibli, T. Residual phase noise suppression for Pound-Drever-Hall cavity stabilization with an electro-optic modulator. *OSA Continuum* **1**, 116–123 (2018).
59. Li, L., Huie, W., Chen, N., Demarco, B. & Covey, J. Active cancellation of servo-induced noise on stabilized lasers via feedforward. *Phys. Rev. Appl.* **18**, 064005 (2022).
60. Chao, Y. et al. Pound-Drever-Hall feedforward: laser phase noise suppression beyond feedback. *Optica* **11**, 945–950 (2024).
61. Levine, H. et al. Parallel implementation of high-fidelity multiqubit gates with neutral atoms. *Phys. Rev. Lett.* **123**, 170503 (2019).
62. Jandura, S. & Pupillo, G. Time-optimal two-and three-qubit gates for Rydberg atoms. *Quantum* **6**, 712 (2022).
63. Fu, Z. et al. High-fidelity entanglement of neutral atoms via a Rydberg-mediated single-modulated-pulse controlled-phase gate. *Phys. Rev. A* **105**, 042430 (2022).
64. Evered, S. et al. High-fidelity parallel entangling gates on a neutral atom quantum computer. *Nature* **622**, 268–272 (2023).
65. Jiang, L. et al. Repetitive readout of a single electronic spin via quantum logic with nuclear spin ancillae. *Science* **326**, 267–272 (2009).
66. Fuhrmanek, A., Bourgain, R., Sortais, Y. & Browaeys, A. Free-space lossless state detection of a single trapped atom. *Phys. Rev. Lett.* **106**, 133003 (2011).
67. Briegel, H., Browne, D., Dür, W., Raussendorf, R. & Vandennest, M. Measurement-based quantum computation. *Nat. Phys.* **5**, 19–26 (2009).
68. Levine, H. et al. Dispersive optical systems for scalable Raman driving of hyperfine qubits. *Phys. Rev. A* **105**, 032618 (2022).
69. Martinez-dorantes, M. et al. Fast nondestructive parallel readout of neutral atom registers in optical potentials. *Phys. Rev. Lett.* **119**, 180503 (2017).
70. Kwon, M., Ebert, M., Walker, T. & Saffman, M. Parallel low-loss measurement of multiple atomic qubits. *Phys. Rev. Lett.* **119**, 180504 (2017).
71. Defenu, N. et al. Long-range interacting quantum systems. *Rev. Mod. Phys.* **95**, 035002 (2023).
72. Choi, J. et al. Robust dynamic Hamiltonian engineering of many-body spin systems. *Phys. Rev. X* **10**, 031002 (2020).
73. Scholl, P. et al. Microwave engineering of programmable XXZ Hamiltonians in arrays of Rydberg atoms. *PRX Quantum* **3**, 020303 (2022).
74. Anand, S. et al. Data and plotting code for 'A dual-species Rydberg array'. *Zenodo* https://doi.org/10.5281/zenodo.12775187 (2024).

Data availability

The data underlying these experiments are available via Zenodo at https://doi.org/10.5281/zenodo.12775187 (ref. 74).

Acknowledgements

We thank S. Weber for helpful discussions regarding the use of the Pairinteraction software package and thank H. Levine for a critical reading of the manuscript. We acknowledge funding from the Office of Naval Research (Grant No. N00014-23-1-2540), the Air Force Office of Scientific Research (Grant Nos. FA9550-21-1-0209 and 22-RI-EP-19) and the National Science Foundation's Quantum Leap Challenge Institute for Hybrid Quantum Architectures and Networks (NSF Award No. 2016136). This material is based upon work supported by the US Department of Energy Office of Science National Quantum Information Science Research Centers. R.W. is supported by a National Science Foundation graduate research fellowship (Grant No. 2140001).

Author contributions

S.A., C.E.B., R.W., V.R., K.S. and H.B. contributed to the experiments, the analysis of the results and the preparation of the manuscript. K.S. and H.B. supervised the experiments.

Competing interests

The authors declare no competing interests.

Additional information

Supplementary information The online version contains supplementary material available at https://doi.org/10.1038/s41567-024-02638-2.

Correspondence and requests for materials should be addressed to Hannes Bernien.

Peer review information *Nature Physics* thanks the anonymous reviewers for their contribution to the peer review of this work.